ACS OMEGA

Open Access

http://pubs.acs.org/journal/acsodf

Article

Coexistence of Ferromagnetism and Ferroelectricity in Cu-Intercalated Bilayer CrI_3

Zhonghua Qian,* Yanbiao Wang,* Jinlian Lu, Ziyu Wang, Xue Rui, Tianying Zhu, Baopei Hua, Guanjie Gu, Qiyuan Peng, and Nini Guo*

Cite This: *ACS Omega* 2024, 9, 11478−11483

Read Online

ACCESS | Metrics & More | Article Recommendations | Supporting Information

ABSTRACT: Design of two-dimensional (2D) multiferroic materials with two or more ferroic orders in one structure is highly desired in view of the development of next-generation electronic devices. Unfortunately, experimental or theoretical discovery of 2D intrinsic multiferroic materials is rare. Using first-principles calculation methods, we report the realization of multiferroics that couple ferromagnetism and ferroelectricity by intercalating Cu atoms in bilayer CrI_3, Cu_x@bi-CrI_3 (x = 0.03, 0.06, and 0.25). Our results show that the intercalation of Cu atoms leads to the inversion symmetry breaking of bilayer CrI_3 and produces intercalation density-dependent out-of-plane electric polarization, around 18.84−90.31 pC·cm^{-2}. Moreover, the switch barriers of Cu_x@bi-CrI_3 in both polarization states are small, ranging from 0.31 to 0.69 eV. Furthermore, the magnetoelectric coupling properties of Cu_x@bi-CrI_3 can be modulated via varying the metal ion intercalation density, and half-metal to semiconductor transition can be occurred by decreasing the intercalation density of metal ions. Our work paves a practical path for 2D magnetoelectron coupling devices.

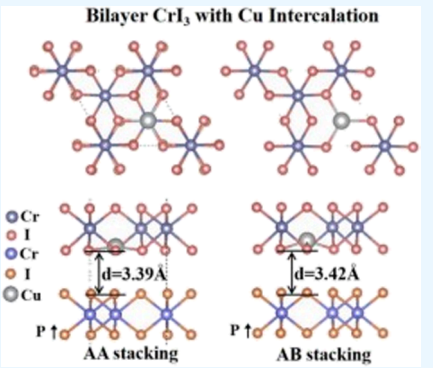

INTRODUCTION

Multiferroics are defined as materials that exhibit two or more primary ferroic features in a single phase, including ferromagnetic/antiferromagnetic (FM/AFM), ferroelectric/antiferroelectric (FE/AFE), ferroelastic orders, etc.[1−11] Among them, magnetoelectric materials, displaying both long-range polarity and magnetic orders, are arguably the most studied multiferroic materials. A number of materials with intrinsic multiferroicity have been synthesized experimentally and predicted theoretically, such as $Sr_3Co_2Fe_{24}O_{41}$,[9] $BiTiO_3$,[10] $CuFe_2O_4$,[11] etc., which hold promising applications for multifunctional devices for low-power, high-density, nonvolatile data storage,[9] sensors,[12] energy harvesting,[13] actuators,[14] etc. Nevertheless, most multiferroic materials face significant technological challenges in terms of downsizing and integration, prompting scientists to seek out low-dimensional multiferroic materials with an atomic thickness.

Interestingly, two-dimensional (2D) multiferroic films have been proposed theoretically and experimentally, such as $CuCrP_2S_6$,[3,4] γ-AlOOH,[6] AgF_2,[7] $FeHfSe_3$,[8] etc. Unfortunately, the variety of 2D intrinsic multiferroic materials is rather rare. Currently, numerous strategies have been proposed to achieve multiferroic materials, including doping FE compounds with magnetic transition metal (TM) ions,[15−17] composing FM monolayers and FE monolayers to form 2D multiferroic heterostructures,[18−24] sliding two FM monolayers to achieve electric control of magnetism,[25,26] etc. In addition, the intercalation method by intercalating atoms,[27−35] ions,[36,37] or molecules[38] has been determined to be an effective method to modulate the physical properties of 2D layered materials.[27−38] For example, Tu and Wu found that inserting 3d TM atoms in layered MoS_2 and Bi_2Se_3 could induce switchable vertical polarization as well as electrically tunable magnetism.[31] Wang et al.[36] and Weber et al.[37] found that the Curie temperatures of 2D Fe_3GeTe_2 and $Cr_2Ge_2Te_6$ can be enhanced as high as ∼300 K by inserting Na and organic ions. Additionally, TaS_2 sheets intercalated with Fe atoms using a chemical vapor transport method show tunable magnetic order, magnetic anisotropy, magnetoresistance, etc.[33−35] Despite the process, theoretical and experimental efforts on the property manipulation of 2D layered materials by intercalation are still limited.

In this work, we designed 2D multiferroic Cu_x@bi-CrI_3 (x = 0.03, 0.06, and 0.25) by inserting Cu ions into bilayer CrI_3 by density functional theory (DFT) calculations. It is found that the intercalation of Cu ions breaks the inversion symmetry of bilayer CrI_3, producing a switchable out-of-plane electron polarization, around 18.84−90.31 pC·cm^{-2}. In particular, by decreasing the intercalation density of metal ions, the

Received: October 24, 2023
Revised: January 30, 2024
Accepted: February 21, 2024
Published: March 1, 2024

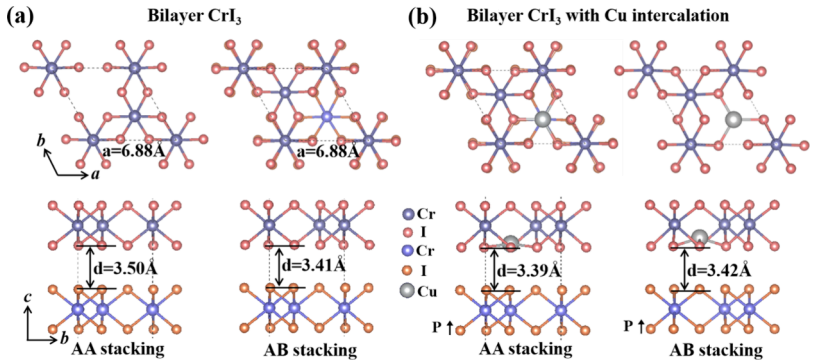

Figure 1. Top and side views of the geometrical structures of AA- and AB-stacked bilayer CrI_3 without (a) and with (b) Cu intercalation.

electronic properties can be changed, resulting in a half-metal to semiconductor transition.

COMPUTATIONAL METHODS

The DFT-based calculations were carried out by Vienna Ab initio Simulation Package (VASP)[39,40] for searching the lowest-energy doping site and electronic properties of the CrI_3 bilayer. The exchange-correlation energy was described by the Perdew−Burke−Ernzerhof functional[41] for the generalized gradient approximation. And the DFT-D2 functional is used to account for the van der Waals interaction.[42] For describing the strong electron correlation between the 3d electrons, the Hubbard U correction of U_{eff} was considered to describe the on-site repulsion interaction of the Cr and Cu ions. We tested the influence of U_{eff} values on the electronic properties of $Cu_{0.25}$@AA-CrI_3; as shown in Table S1 and Figure S1 in the Supporting Information, U_{eff} = 2.0 eV and U_{eff} = 3.0 eV obtain the same results. Therefore, we use U_{eff} = 2.0 eV for all of the calculations. The energy cutoff was set as 450 eV. The energy and force convergence thresholds for the iteration in the self-consistent field were set to 10^{-6} eV and 0.01 eV/Å, respectively. The vacuum layer of about 20 Å along the c-direction was adopted to avoid the interaction between two periodic units. The polarization is obtained by the modern theory of polarization based on the Berry-phase approach with dipole correction,[43,44] and the climbing image nudged elastic band (cNEB)[45,46] method was employed to calculate the minimum energy path and diffusion energy barriers.

RESULTS AND DISCUSSION

As shown in Figure 1a, two types of stacking configurations for bilayer CrI_3 were considered, namely, AA-stacking and AB-stacking configurations, respectively. Both configurations are found to have nearly degenerated energies with identical lattice parameters (a = 6.88 Å) and interlayer distances (d = 3.41 Å). As both AA and AB stackings may be prepared in the experiments,[47] in this work, we will investigate the effect of metal insertion on the electronic properties in both AA- and AB-stacking structures. Our results show that bilayer CrI_3 in both stacking configurations favors FM order, which is about 0.34 and 4.43 meV/Cr atom lower than the AFM state for AA- and AB-stacking configurations, respectively (see Table S2 in the Supporting Information). These results are consistent with previous experimental observations.[30,47]

Next, we explored the possibility of intercalating Cu atoms into AA- and AB-stacking bilayer CrI_3. First, the unit cell of bilayer CrI_3 is selected to intercalate Cu atoms. Here, the intercalated structure is described as $Cu_{0.25}$@AA-CrI_3 and $Cu_{0.25}$@AB-CrI_3 for AA and AB stackings, respectively, wherein the ratio of intercalated Cu atom to Cr atom is 1:4. We considered four types of intercalation configurations, denoted as Inter-I, Inter-II, Inter-III, and Inter-IV, as shown in Figure S2: (i) Inter-I—the Cu atom sits in the middle of two CrI_3 layers and facing the Cr atoms in the upper and lower layers. (ii) Inter-II—the Cu atom sits on the middle of three I atoms of one CrI_3 layer and facing a I atom of another CrI_3 layer. (iii) Inter-III—the Cu atom is located in the middle of the two sublayers, facing the hollow site of one CrI_3 layer and a Cr atom of another CrI_3 layer (directly facing the hollow site in the upper and lower layers in AA stacking). (iv) Inter-IV—the Cu atom sits in the hollow site of one CrI_3 layer and facing the Cr atom of another CrI_3 layer (facing another hollow site of another CrI_3 layer in AA stacking). Upon optimization, the Inter-VI configuration is the most favored structure for both $Cu_{0.25}$@AA-CrI_3 and $Cu_{0.25}$@AB-CrI_3 (see Table S3). As shown in Figure 1b, the intercalated Cu atom locates in the hollow site of one CrI_3 sublayer and sits in the same plane of the I atom layer. The distance of the Cu atom to the opposite CrI_3 layer is about 4.10 and 4.01 Å in $Cu_{0.25}$@AA-CrI_3 and $Cu_{0.25}$@AB-CrI_3, respectively. To characterize the energetic stability of intercalated systems, we define the intercalation energy as

$$E_{int} = E_{tot} - E_{bilayer} - E_{Cu} \quad (1)$$

Here, E_{tot} and $E_{bilayer}$ are the energies of the CrI_3 bilayer with and without intercalation, respectively, and E_{Cu} is the energy of the single Cu atom. The calculated E_{int} values are −3.15 and −3.10 eV for $Cu_{0.25}$@AA-CrI_3 and $Cu_{0.25}$@AB-CrI_3, respectively (see Table 1), which are comparable with the Fe/Co intercalated BN/MoS_2 system.[48] The negative energies indicate that the intercalation of Cu atoms in the CrI_3 bilayer is an exothermic reaction. As shown in Figure 1b, the inversion symmetry of Cu-intercalated bilayer CrI_3 in both stackings is

Table 1. Intercalation Energy E_{int} (eV), Band Gap E_g (eV), Switch Barrier Δ (eV), and Vertical Polarization P_z (pC·cm^{-2}) of Cu-Intercalated Bilayer CrI_3

	E_{int} [eV]	E_g [eV]	Δ [eV]	P_z [pC·cm^{-2}]
$Cu_{0.25}$@AA-CrI_3	−3.15	half metal	0.43	90.31
$Cu_{0.06}$@AA-CrI_3	−3.17	half metal	0.49	80.45
$Cu_{0.03}$@AA-CrI_3	−3.20	0.81	0.49	47.57
$Cu_{0.25}$@AB-CrI_3	−3.10	half metal	0.64	20.01
$Cu_{0.06}$@AB-CrI_3	−3.16	half metal	0.31	30.21
$Cu_{0.03}$@AB-CrI_3	−3.13	0.86	0.69	18.84

https://doi.org/10.1021/acsomega.3c08360
ACS Omega 2024, 9, 11478−11483

broken, which leads to positive and negative charge centers' spatial separation along the out-of-plane direction and results in the unequal electrostatic potential of the top and bottom CrI_3 layer. Moreover, as the Cu atom is located in the hollow site of the top CrI_3 sublayer (see Figure 1b), it results in a positive charge center moving up and forms an upward FE polarization (P↑) with the values of 20.01 and 90.31 pC·cm^{-2} in AA- and AB-stacking configurations, respectively (see Table 1).

Furthermore, to demonstrate the feasibility of the reversal of the FE polarization direction in $Cu_{0.25}$@AA-CrI_3 and $Cu_{0.25}$@AB-CrI_3, the energy barrier using the cNEB method is explored (shown in Figure 2a,b). In the AA-stacking configuration, the

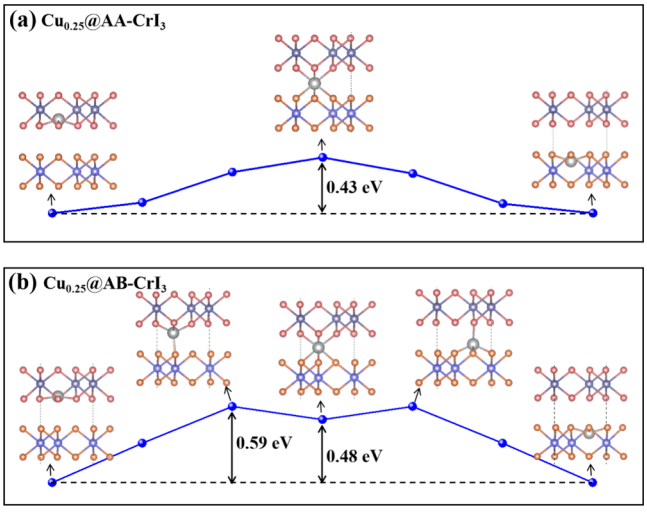

Figure 2. FE switching pathway of (a) $Cu_{0.25}$@AA-CrI_3 and (b) $Cu_{0.25}$@AB-CrI_3. The values denote the transition barrier between the two switchable FE states.

Cu ion in the hollow site of the upper CrI_3 sublayer forms an upward FE polarization (P↑). When adding an external electric field, the Cu ion moves straightly downward to form an Inter-III configuration without FE polarization. If the external electric field continues to increase, the Cu ion continues to move downward, ending up in the hollow site of the lower CrI_3 sublayer and forming a downward FE polarization (P↓). In the AB-stacking one (see Figure 2b), the external electric field turns the Inter-IV configuration to the Inter-II configuration, then the Inter-I configuration forms the paraelectric phase (PE), and finally the Cu ion moves downward to the hollow site of the lower CrI_3 sublayer and the direction of FE polarization has been switched. The switching barriers are 0.43 and 0.59 eV per Cu ion for AA- and AB-stacking configurations, respectively, which are comparable to that of reported $Cr_{0.5}MoS_2$.[31]

Figure 3 shows the band structure and projected density of states (PDOS) of $Cu_{0.25}$@AA-CrI_3 and $Cu_{0.25}$@AB-CrI_3 in two FE states. In the case of AA-stacking configuration, $Cu_{0.25}$@AA-CrI_3 is FM half metal in both polarized states, in which the spin-up electrons are conducting while spin-down electrons are insulating with a band gap of 2.48 eV both in the P↑ and P↓ states. The energy differences between FM and interlayer AFM states are listed in Table S4. Similar electronic properties are found for those in the AB-stacking configuration, in which the band gap of the spin-down channel is 2.38 eV in both P↑ and P↓ states. The electronic properties of $Cu_{0.25}$@AA-CrI_3 and $Cu_{0.25}$@AB-CrI_3 are different with that of bilayer CrI_3 reported by Liu's group,[49] in which the AA-stacking and AB-stacking bilayer CrI_3 are insulating with the gaps of 0.81 and 0.82 eV, respectively. The insets in Figure 3a−d are spin density plots. Clearly, the magnetic moments of the systems are mainly contributed by the Cr atom; in contrast, the intercalated Cu ions are nonmagnetic. As shown in charge density difference plots in Figure S3, the Cu ions are electron donors, which contribute charges to the I atoms from the nearest CrI_3 sublayer, leading to the increase of the local magnetic moment of the Cr ions from 3.29 to 3.55 μ_B in AA- and AB-stacking configurations. For the CrI_3 sublayer far away from the Cu ions, the local magnetic moments of Cr ions remain almost unchanged with that in bilayer CrI_3, ∼3.29 μ_B for AA- and AB-stacking configurations.

Compared with free-standing bilayer CrI_3, the Fermi levels of $Cu_{0.25}$@AA-CrI_3 and $Cu_{0.25}$@AB-CrI_3 in both polarization states are upshifted and cross the Fermi level of the spin-up channel due to the electron transfer occurring from the Cu atom to CrI_3 sublayer. As seen from the PDOS plots, the valence band maximum (VBM) of $Cu_{0.25}$@AA-CrI_3 and $Cu_{0.25}$@AB-CrI_3 is mainly contributed by the CrI_3 sublayer close to the intercalated Cu ion, and the conduction band minimum (CBM) is mainly from the CrI_3 sublayer far away from the Cu atom. Therefore, the built-in electric field induced by the intercalated Cu atom can tune the electronic and magnetic properties of the CrI_3 bilayer.

Furthermore, the influence of the intercalation density of Cu ions on the electronic and magnetic properties of bilayer CrI_3 is explored. Here, we constructed the intercalated structures with larger supercells of bilayer CrI_3 (2 × 2 and 3 × 3 supercells), which have a lower metal intercalation density, namely, $Cu_{0.06}$@AA(AB)-CrI_3 and $Cu_{0.03}$@AA(AB)-CrI. Compared with $Cu_{0.25}$@AA(AB)-CrI_3, the distance of the Cu atom to the opposite CrI_3 layer is smaller, around 0.15/0.20 and 0.18/0.19 Å in $Cu_{0.06}$@AA/AB-CrI_3 and $Cu_{0.03}$@AA/AB-CrI_3, respectively. Moreover, the polarization of the intercalated systems weakens with the decrease of the intercalation density (see Table 1). The polarization values of $Cu_{0.06}$@AA-CrI_6 and $Cu_{0.06}$@AB-CrI_3 are 80.45 and 47.57 pC·cm^{-2}, respectively, while those of $Cu_{0.03}$@AA-CrI_3 and $Cu_{0.03}$@AB-CrI_3 are reduced to 30.21 and 18.84 pC·cm^{-2}, respectively. The switching barriers are 0.49/0.44 and 0.49/0.47 eV for $Cu_{0.06}$@AA/AB-CrI_3 and $Cu_{0.03}$@AA/AB-CrI_3, respectively (see Figures S4 and S5). Moreover, the Fermi level decreases with the decrease in intercalated Cu metal concentration. As shown in the PDOS plots in Figure 4, $Cu_{0.06}$@AA/AB-CrI_3 are half metals with small electronic states crossing the Fermi level, which are turned to be semiconductors for $Cu_{0.03}$@AA/AB-CrI_3 in both stackings, and the band gaps are 0.55 and 0.66 eV for $Cu_{0.06}$@AA/AB-CrI_3, respectively. Our results show that the electronic property of Cu_x@AA/AB-CrI_3 can be effectively modulated by changing the intercalated Cu atom concentration.

CONCLUSIONS

By using first-principles calculations, we systematically studied the magnetoelectronic coupling properties of Cu-intercalated bilayer CrI_3 in both AA and AB stackings, Cu_x@AA/AB-CrI_3 (x = 0.03, 0.06, and 0.25). Our results show that the intercalant can induce a spontaneous inversion symmetry breaking, and the polarization values of $Cu_{0.25}$@AA-CrI_3 and $Cu_{0.25}$@AB-CrI_3 are 20.01 and 90.31 pC·cm^{-2}, respectively. The switching

https://doi.org/10.1021/acsomega.3c08360
ACS Omega 2024, 9, 11478−11483

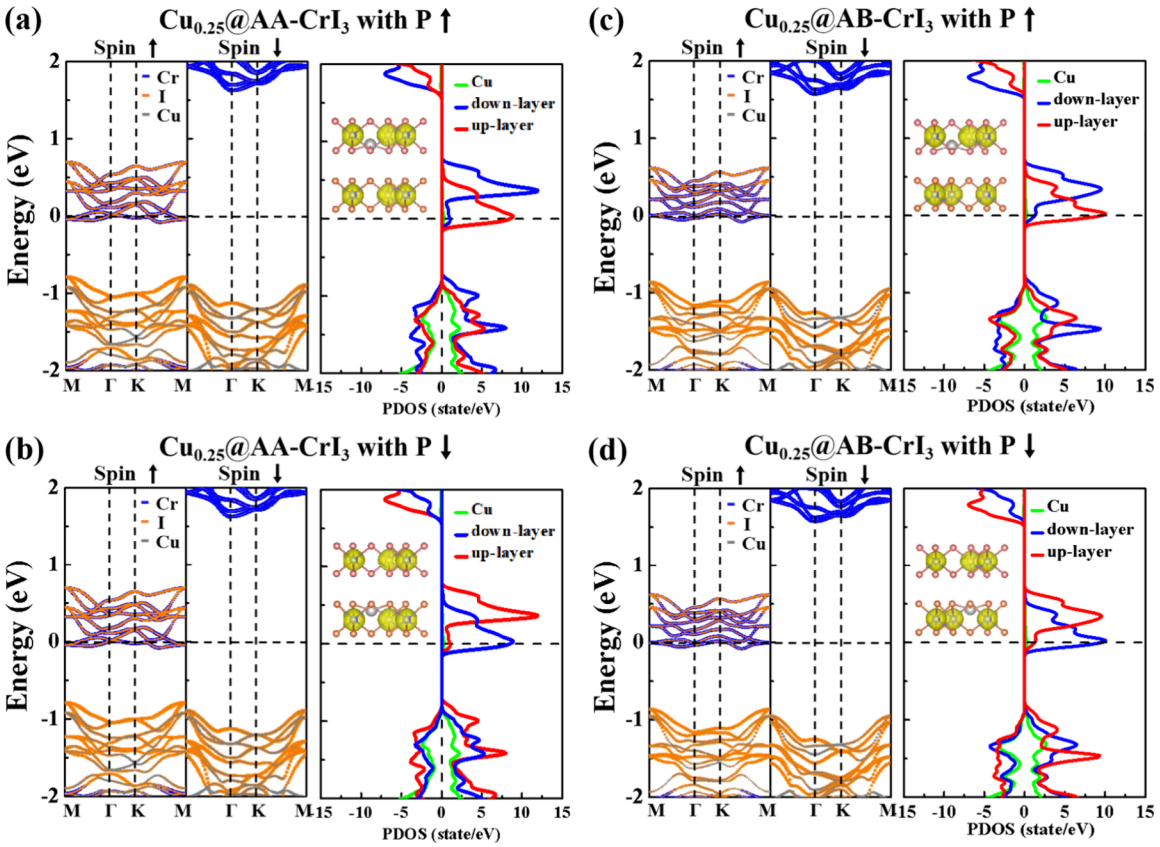

Figure 3. Band structure (left) and PDOS (right) of (a) $Cu_{0.25}$@AA-CrI_3 (P↑), (b) $Cu_{0.25}$@AA-CrI_3 (P↓), (c) $Cu_{0.25}$@AB-CrI_3 (P↑), and (d) $Cu_{0.25}$@AB-CrI_3 (P↓), respectively. The insets are the spin density distributions.

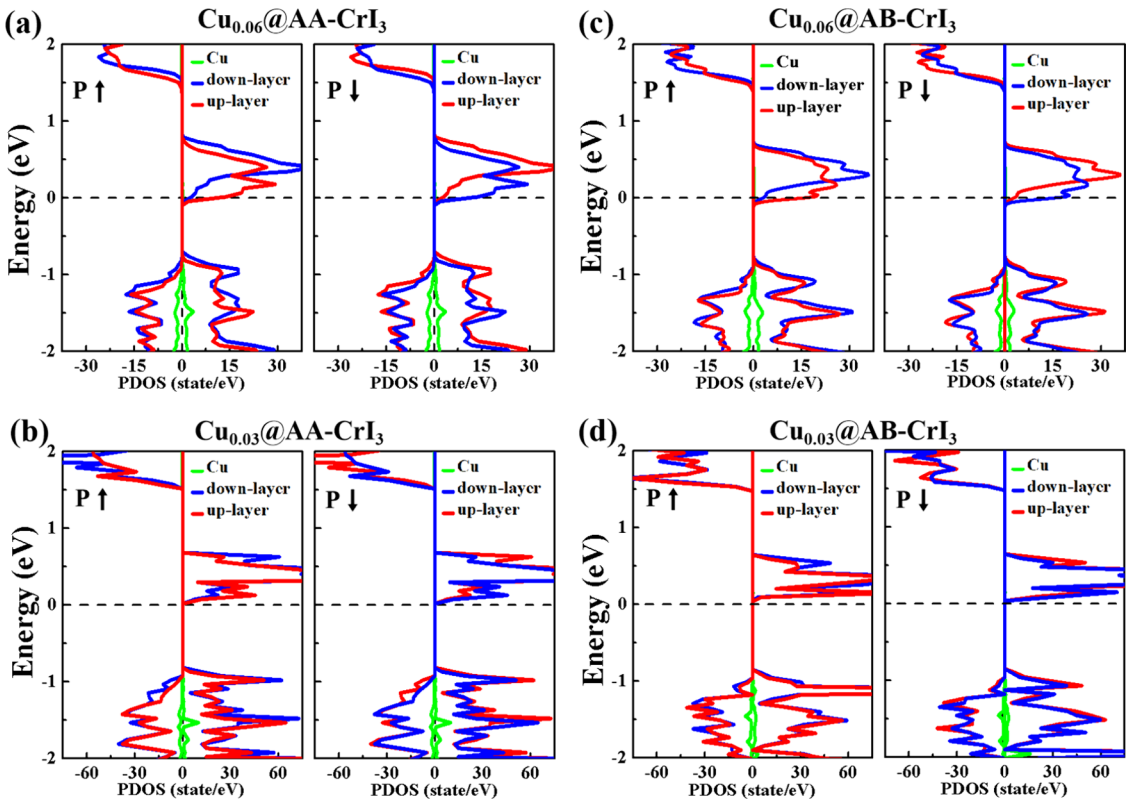

Figure 4. PDOS of (a) $Cu_{0.06}$@AA-CrI_3, (b) $Cu_{0.03}$@AA-CrI_3, (c) $Cu_{0.06}$@AB-CrI_3, and (d) $Cu_{0.03}$@AB-CrI_3 in switchable polarization states, respectively.

https://doi.org/10.1021/acsomega.3c08360
ACS Omega 2024, 9, 11478−11483

barriers are 0.43 and 0.59 eV per Cu ion in $Cu_{0.25}$@AA-CrI_3 and $Cu_{0.25}$@AB-CrI_3, respectively. Moreover, the electronic properties of Cu_x@AA/AB-CrI_3 are found to be sensitive to the metal ion density. By decreasing the intercalation concentration, a half-metal to semiconductor transition occurs. Our study provides a promising way to design 2D multiferroics.

■ ASSOCIATED CONTENT

Supporting Information

The Supporting Information is available free of charge at https://pubs.acs.org/doi/10.1021/acsomega.3c08360.

> Influence of U_{eff} values on the electronic properties of $Cu_{0.25}$@AA-CrI_3; band structures of (a) $Cu_{0.25}$@AA-CrI_3 and $Cu_{0.25}$@AB-CrI_3; energy difference of bilayer CrI_3 in AA and AB stackings; four configurations with different interpolation positions in two-stacking bilayer CrI_3; energy difference of four configurations with different interpolation positions in two-stacking bilayer CrI_3; energy difference between FM and interlayer AFM states of Cu_x@AA-CrI_3; top and side views of the charge density difference plots of $Cu_{0.25}$@AA-CrI_3 and $Cu_{0.25}$@AB-CrI_3; FE switching pathway of $Cu_{0.06}$@AA-CrI_3 and $Cu_{0.06}$@AB-CrI_3; FE switching pathway of $Cu_{0.03}$@AA-CrI_3 and $Cu_{0.03}$@AB-CrI_3 (PDF)

■ AUTHOR INFORMATION

Corresponding Authors

Zhonghua Qian − *College of Physics Science and Technology, Yangzhou University, Yangzhou 225002, China;* orcid.org/0009-0008-5639-050X; Email: qianzh@yzu.edu.cn

Yanbiao Wang − *Department of Fundamental Courses, Wuxi Institute of Technology, Wuxi 214121, China;* Email: wangyb@wxit.edu.cn

Nini Guo − *College of Physics and Hebei Advanced Thin Films Laboratory, Hebei Normal University, Shijiazhuang 050024, China*; Email: guonini981213@163.com

Authors

Jinlian Lu − *Department of Physics, Yancheng Institute of Technology, Yancheng, Jiangsu 224051, China*

Ziyu Wang − *College of Physics Science and Technology, Yangzhou University, Yangzhou 225002, China*

Xue Rui − *College of Physics Science and Technology, Yangzhou University, Yangzhou 225002, China*

Tianying Zhu − *College of Physics Science and Technology, Yangzhou University, Yangzhou 225002, China*

Baopei Hua − *College of Physics Science and Technology, Yangzhou University, Yangzhou 225002, China*

Guanjie Gu − *College of Physics Science and Technology, Yangzhou University, Yangzhou 225002, China*

Qiyuan Peng − *College of Physics Science and Technology, Yangzhou University, Yangzhou 225002, China*

Complete contact information is available at: https://pubs.acs.org/10.1021/acsomega.3c08360

Notes

The authors declare no competing financial interest.

■ ACKNOWLEDGMENTS

This work is supported by the National Natural Science Foundation of China (41975062).

■ REFERENCES

(1) Gao, Y.; Gao, M.; Lu, Y. Two-dimensional multiferroics. *Nanoscale* **2021**, *13*, 19324−19340.

(2) Behera, B.; Sutar, B. C.; Pradhan, N. R. Recent progress on 2D ferroelectric and multiferroic materials, challenges, and opportunity. *Emerg. Mater.* **2021**, *4*, 847−863.

(3) Lai, Y.; Song, Z.; Wan, Y.; Xue, M.; Wang, C.; Ye, Y.; Dai, L.; Zhang, Z.; Yang, W.; Du, H.; Yang, J. Two-dimensional ferromagnetism and driven ferroelectricity in van der Waals $CuCrP_2S_6$. *Nanoscale* **2019**, *11*, 5163−5170.

(4) Zhang, D.; Li, A.; Chen, X.; Zhou, W.; Ouyang, F. Tuning valley splitting and magnetic anisotropy of multiferroic $CuMP_2X_6$ (M = Cr,V;X = S,Se) monolayer. *Phys. Rev. B* **2022**, *105*, No. 085408.

(5) Tan, H.; Li, M.; Liu, H.; Liu, Z.; Li, Y.; Duan, W. Two-dimensional ferromagnetic-ferroelectric multiferroics in violation of the d^0 rule. *Phys. Rev. B* **2019**, *99*, No. 195434.

(6) Liu, C.; Gao, R.; Cheng, X.; Yang, X.; Qin, G.; Gao, H.; Picozzi, S.; Ren, W. First-principles study of ferroelectricity, antiferroelectricity, and ferroelasticity in two-dimensional γ-AlOOH. *Phys. Rev. B* **2023**, *107*, L121402.

(7) Xu, X.; Ma, Y.; Zhang, T.; Lei, C.; Huang, B.; Dai, Y. Prediction of two-dimensional antiferromagnetic ferroelasticity in an AgF_2 monolayer. *Nanoscale Horiz* **2020**, *5*, 1386−1393.

(8) Yu, S.; Wang, Y.; Wang, S.; Zhang, H.; Huang, B.; Dai, Y.; Wei, W. Robust Intrinsic Multiferroicity in a $FeHfSe_3$ Layer. *J. Phys. Chem. Lett.* **2021**, *12*, 8882−8888.

(9) Zhai, K.; Shang, D.; Chai, Y.; Li, G.; Cai, J.; Shen, B.; Sun, Y. Room-Temperature Nonvolatile Memory Based on a Single-Phase Multiferroic Hexaferrite. *Adv. Funct. Mater.* **2017**, *28*, 1705771.

(10) Revathy, R.; Thankachan, R. M.; Kalarikkal, N.; Varma, M. R.; Surendran, K. P. Sea urchin-like Ni encapsulated with $BaTiO_3$ to form multiferroic core-shell structures for room temperature magnetoelectric sensors. *J. Alloys Compd.* **2021**, *881*, No. 160579.

(11) Rahul, M. T.; Chacko, S. K.; Vinodan, K.; Raneesh, B.; Philip K, A.; Bhadrapriya, B. C.; Bose, B. A.; Kalarikkal, N.; Rouxel, D.; Viswanathan, P.; Chandrasekhar, A. Multiferroic and energy harvesting characteristics of P(VDF-TrFE)-$CuFe_2O_4$ flexible films. *Polymer* **2022**, *252*, No. 124910.

(12) Bichurin, M.; Petrov, R.; Leontiev, V.; Semenov, G.; Sokolov, O. Magnetoelectric Current Sensors. *Sensors* **2017**, *17*, 1271.

(13) Yang, Z.; Zhou, S.; Zu, J.; Inman, D. High-Performance Piezoelectric Energy Harvesters and Their Applications. *Joule* **2018**, *2*, 642−697.

(14) Hiremath, N.; Guntupalli, R.; Vodyanoy, V.; Chin, B. A.; Park, M.-K. Detection of methicillin-resistant Staphylococcus aureus using novel lytic phage-based magnetoelastic biosensors. *Sen. Actuators B Chem.* **2015**, *210*, 129−136.

(15) Zhang, D.; Zhou, B. Conduction band-edge valley splitting in two-dimensional ferroelectric $AgBiP_2S_6$ by magnetic doping: towards electron valley-polarized transport. *RSC Adv.* **2022**, *12*, 13765−13773.

(16) Liu, Y.; Zhou, W.; Tang, G.; Yang, C.; Wang, X.; Hong, J. Coexistence of Magnetism and Ferroelectricity in 3*d* Transition-Metal-Doped SnTe Monolayer. *J. Phys. Chem. C* **2019**, *123*, 28919−28924.

(17) Pang, K.; Xu, X.; Ku, R.; Wei, Y.; Ying, T.; Li, W.; Yang, J.; Li, X.; Jiang, Y. Ferroelectricity and High Curie Temperature in a 2D Janus Magnet. *ACS Appl. Mater. Interfaces* **2023**, *15*, 10133−10140.

(18) Lu, J.; Guo, N.; Duan, Y.; Wang, S.; Mao, Y.; Yi, S.; Meng, L.; Yao, X.; Zhang, X. The effect of switchable electronic polarization states on the electronic properties of two-dimensional multiferroic $TMBr_2/Ga_2SSe_2$ (TM = V-Ni) heterostructures. *Phys. Chem. Chem. Phys.* **2023**, *25*, 21227−21235.

(19) Zhang, X.; Zhou, Z.; Yu, X.; Guo, Y.; Chen, Y.; Wang, J. Ferroelectric Control of Polarity of the Spin-polarized Current in Van

Der Waals Multiferroic Heterostructures. *Adv. Funct. Mater.* **2023**, *33*, 2301353.
(20) Guo, N.; Zhu, X.; Lian, H.; Guo, T.; Wang, Z.; Zhang, H.; Yao, X.; Wang, B.; Zhang, X. 2D $CrMoC_2S_6/Sc_2CO_2$ multiferroic heterostructure with robust antiferromagnetic ordering, switchable electronic properties and magnetic anisotropy. *J. Alloys Compd.* **2023**, *952*, No. 169962.
(21) Yang, F.; Shang, J.; Kou, L.; Li, C.; Deng, Z. Controllable Valley Polarization and Strain Modulation in 2D 2H-$VS_2/CuInP_2Se_6$ Heterostructures. *Nanomaterials* **2022**, *12*, 2461.
(22) Wang, Y.; Xu, X.; Zhao, X.; Ji, W.; Cao, Q.; Li, S.; Li, Y. Switchable half-metallicity in A-type antiferromagnetic NiI2 bilayer coupled with ferroelectric In_2Se_3. *npj Comput. Mater.* **2022**, *8*, 218.
(23) Liu, X.; Shen, C.; Li, X.; Wang, T.; He, M.; Li, L.; Wang, Y.; Li, J.; Xia, C. Magnetoelectric coupling effects on the band alignments of multiferroic In_2Se_3-CrI_3 trilayer heterostructures. *Nanoscale* **2022**, *14*, 5454−5461.
(24) Cao, L.; Deng, X.; Zhou, G.; Liang, S.-J.; Nguyen, C. V.; Ang, L. K.; Ang, Y. S. Multiferroic van der Waals heterostructure $FeCl_2$/Sc_2CO_2: Nonvolatile electrically switchable electronic and spintronic properties. *Phys. Rev. B* **2022**, *105*, No. 165302.
(25) Liu, K.; Ma, X.; Xu, S.; Li, Y.; Zhao, M. Tunable sliding ferroelectricity and magnetoelectric coupling in two-dimensional multiferroic MnSe materials. *npj Comput. Mater.* **2023**, *9*, 16.
(26) Wan, Y.; Hu, T.; Mao, X. Y.; Fu, J.; Yuan, K.; Song, Y.; Gan, X. T.; Xu, X. L.; Xue, M. Z.; Cheng, X.; Huang, C. X.; Yang, J. B.; Dai, L.; Zeng, H. L.; Kan, E. Room-Temperature Ferroelectricity in 1T'-ReS_2 Multilayers. *Phys. Rev. Lett.* **2022**, *128*, No. 067601.
(27) Zhang, L.; Tang, C.; Sanvito, S.; Gu, Y.; Du, A. Hydrogen-Intercalated 2D Magnetic Bilayer: Controlled Magnetic Phase Transition and Half-Metallicity via Ferroelectric Switching. *ACS Appl. Mater. Interfaces* **2022**, *14*, 1800−1806.
(28) Noor-A-Alam, M.; Nolan, M. Engineering Ferroelectricity and Large Piezoelectricity in h-BN. *ACS Appl. Mater. Interfaces* **2023**, *15*, 42737−42745.
(29) Lyu, H. Y.; Zhang, Z.; You, J. Y.; Yan, Q. B.; Su, G. Two-Dimensional Intercalating Multiferroics with Strong Magnetoelectric Coupling. *J. Phys. Chem. Lett.* **2022**, *13*, 11405−11412.
(30) Guo, Y.; Liu, N.; Zhao, Y.; Jiang, X.; Zhou, S.; Zhao, J. Enhanced Ferromagnetism of CrI_3 Bilayer by Self-Intercalation. *Chin. Phys. Lett.* **2020**, *37*, No. 107506.
(31) Tu, Z.; Wu, M. 2D Diluted Multiferroic Semiconductors upon Intercalation. *Adv. Electron. Mater.* **2019**, *5*, 1800960.
(32) Yang, Q.; Xiong, W.; Zhu, L.; Gao, G.; Wu, M. Chemically Functionalized Phosphorene: Two-Dimensional Multiferroics with Vertical Polarization and Mobile Magnetism. *J. Am. Chem. Soc.* **2017**, *139*, 11506−11512.
(33) Zhang, C.; Yuan, Y.; Wang, M.; Li, P.; Zhang, J.; Wen, Y.; Zhou, S.; Zhang, X.-X. Critical behavior of intercalated quasi-van der Waals ferromagnet $Fe_{0.26}TaS_2$. *Phys. Rev. Mater.* **2019**, *3*, No. 114403.
(34) Hardy, W. J.; Chen, C.-W.; Marcinkova, A.; Ji, H.; Sinova, J.; Natelson, D.; Morosan, E. Very large magnetoresistance in $Fe_{0.28}TaS_2$ single crystals. *Phys. Rev. B* **2015**, *91*, No. 054426.
(35) Morosan, E.; Zandbergen, H. W.; Li, L.; Lee, M.; Checkelsky, J. G.; Heinrich, M.; Siegrist, T.; Ong, N. P.; Cava, R. J. Sharp switching of the magnetization in$Fe_{1/4}TaS_2$. *Phys. Rev. B* **2007**, *75*, No. 104401.
(36) Wang, N.; Tang, H.; Shi, M.; Zhang, H.; Zhuo, W.; Liu, D.; Meng, F.; Ma, L.; Ying, J.; Zou, L.; Sun, Z.; Chen, X. Transition from Ferromagnetic Semiconductor to Ferromagnetic Metal with Enhanced Curie Temperature in $Cr_2Ge_2Te_6$ via Organic Ion Intercalation. *J. Am. Chem. Soc.* **2019**, *141*, 17166−17173.
(37) Weber, D.; Trout, A. H.; McComb, D. W.; Goldberger, J. E. Decomposition-Induced Room-Temperature Magnetism of the Na-Intercalated Layered Ferromagnet $Fe_{3-x}GeTe_2$. *Nano Lett.* **2019**, *19*, 5031−5035.
(38) Yang, Q.; Zhong, T.; Tu, Z.; Zhu, L.; Wu, M.; Zeng, X. C. Design of Single-Molecule Multiferroics for Efficient Ultrahigh-Density Nonvolatile Memories. *Adv. Sci.* **2019**, *6*, 1801572.
(39) Kresse, G.; Hafner, J. Ab initio molecular dynamics for open-shell transition metals. *Phys. Rev. B* **1993**, *48*, 13115−13118.
(40) Kresse, G.; Furthmuller, J. Efficiency of ab-initio total energy calculations for metals and semiconductors using a plane-wave basis set. *Comput. Mater. Sci.* **1996**, *6*, 15−50.
(41) Perdew, J. P.; Burke, K.; Ernzerhof, M. Generalized Gradient Approximation Made Simple. *Phys. Rev. Lett.* **1996**, *77*, 3865.
(42) Grimme, S. Semiempirical GGA-type density functional constructed with a long-range dispersion correction. *J. Comput. Chem.* **2006**, *27*, 1787−99.
(43) Bengtsson, L. Dipole correction for surface supercell calculations. *Phys. Rev. B* **1999**, *59*, 12301.
(44) King-Smith, R. D.; Vanderbilt, D. Theory of polarization of crystalline solids. *Phys. Rev. B* **1993**, *47*, 1651.
(45) Jo′nsson, H.; Mills, G.; Jacobsen, K. W. Nudged Elastic Band Method for Finding Minimum Energy Paths of Transitions. *World Sci.* **1998**, *16*, 385−404.
(46) Henkelman, G.; Uberuaga, B. P.; Jonsson, H. A climbing image nudged elastic band method for finding saddle points and minimum energy paths. *J. Chem. Phys.* **2000**, *113*, 9901.
(47) Sivadas, N.; Okamoto, S.; Xu, X.; Fennie, C. J.; Xiao, D. Stacking-Dependent Magnetism in Bilayer CrI_3. *Nano Lett.* **2018**, *18*, 7658−7664.
(48) Liu, F.; Liao, Y.; Wu, Y.; Huang, Z.; Liu, H.; He, C.; Qi, A.; Zhong, J. The electronic and magnetic properties of *h*-BN/MoS_2 heterostructures intercalated with 3*d* transition metal atoms. *Phys. Chem. Chem. Phys.* **2021**, *23*, 506−513.
(49) Liu, X.; Legut, D.; Zhang, Q. Photoinduced Ultrafast Phase Transition in Bilayer CrI_3. *J. Phys. Chem. Lett.* **2023**, *14*, 7744−7750.

https://doi.org/10.1021/acsomega.3c08360
ACS Omega 2024, 9, 11478−11483